Dalton Transactions

Thermodynamic Targeting of Electrocatalytic CO_2 Reduction: Advantages, Limitations, and Insights for Catalyst Design

Journal:	*Dalton Transactions*
Manuscript ID	DT-ART-08-2019-003255.R1
Article Type:	Paper
Date Submitted by the Author:	05-Sep-2019
Complete List of Authors:	Ostericher, Andrew L.; University of California, San Diego Porter, Tyler; University of California, San Diego, Department of Chemistry and Biochemistry Reineke, Mark; University of California, San Diego, Department of Chemistry and Biochemistry Kubiak, Clifford; University of California, San Diego, Department of Chemistry and Biochemistry

Thermodynamic Targeting of Electrocatalytic CO_2 Reduction: Advantages, Limitations, and Insights for Catalyst Design

Andrew L. Ostericher, Tyler M. Porter, Mark H. Reineke, and Clifford P. Kubiak*

Department of Chemistry and Biochemistry, University of California, San Diego, 9500 Gilman Drive, Mail Code 0358, La Jolla, California 92093-0358

ABSTRACT

Herein is reported the electrocatalytic reduction of CO_2 with the complex [Ni(bis-NHC)(dmpe)]$^{2+}$ (**1**) (bis-NHC = 1,1':3,3'-bis(1,3-propanediyl)dibenzimidazolin-2,2'-diylidene; dmpe = 1,2-Bis(dimethylphosphino)ethane). The hydricity of **1** was previously benchmarked to be $\Delta G^{\circ}_{H^-} < 40.6$ kcal mol^{-1}, equating to a driving force of a minimum of ~3.4 kcal mol^{-1} for hydride transfer to CO_2. While hydride transfer to CO_2 is thermodynamically favorable, electrocatalytic and infrared spectroelectrochemical (IR-SEC) experiments reveal that hydride transfer is blocked by direct reactivity with CO_2 in the reduced, Ni(0) state of the catalyst, yielding CO via reductive disproportionation ($2CO_2 + 2e^- = CO + CO_3^{2-}$) and concomitant catalyst degradation. Although thermodynamic scaling relationships provide guidance in catalyst targeting, the findings herein illustrate the fundamental kinetic challenges in balancing substrate reactivity and selectivity in the design of CO_2 reduction electrocatalysts. Advantages and limitations of this scaling relationship as well as approaches by which

divergence from it may be achieved are discussed, which provides insight on important parameters for future catalyst design.

INTRODUCTION

Electrochemical reduction of CO_2 to value-added products represents an attractive approach to mitigating the adverse effects of anthropogenic emission of CO_2 while simultaneously manufacturing economically desirable products.[1-5] The two-electron, two-proton reduction of CO_2 to carbon monoxide or formic acid, are two pathways of particular interest due to their applications in Fischer-Tropsch and formic acid fuel cells, respectively.[4, 6] Our lab and others have studied homogeneous metal hydride tuning as a means of targeting efficient catalysts for CO_2 reduction and the hydrogen evolution reaction (HER).[7-15] Hydricity ($\Delta G°_{H-}$), is the propensity of hydride transfer from a hydride donor and plays a key role in determining the subsequent reactivity of the metal hydride donor with a given substrate, whether the substrate is CO_2 or protons in the cases of CO_2 reduction or HER, respectively. While thermodynamically favorable hydrogen evolution is dependent on the pK_a of the acid substrate relative to hydricity of the hydride, thermodynamically favorable hydride transfer from a metal hydride to CO_2 to produce formate requires the hydricity of the hydride donor to be stronger than formate ($\Delta G°_{H-} < 44$ kcal mol^{-1} in acetonitrile).[12] (Scheme 1)

Scheme 1. Thermochemical cycle for hydride transfer to CO_2.

$$[M\text{-}H]^{(n-1)+} \rightleftharpoons M^{n+} + H^- \qquad \Delta G^\circ_{H^-} \qquad (1)$$

$$CO_2 + H^- \rightleftharpoons HCO_2^- \qquad -\Delta G^\circ_{H^-}(HCO_2^-) \qquad (2)$$

$$[M\text{-}H]^{(n-1)+} + CO_2 \rightleftharpoons M^{n+} + HCO_2^- \qquad \Delta G^\circ_{Rxn} \qquad (3)$$

$$\Delta G^\circ_{Rxn} = \Delta G^\circ_{H^-}([M\text{-}H]^{(n-1)}) - \Delta G^\circ_{H^-}(HCO_2^-) \qquad (4)$$

In an effort to tune and target hydride donors to catalyze CO_2 reduction, our lab has recently expanded on a useful scaling relationship that was initially noted by Berning *et al.* in 2001 between hydricity and the first reduction potential of the parent metal complex ($E_{1/2}(M^{n+/(n-1)+})$) (Figure 1). [16, 17] This relationship is expressed in *eq* 8 (Scheme 2), and it provides a means of predicting hydricity based on $E_{1/2}(M^{n+/(n-1)+})$, and establishes criteria for targeting highly reactive transition metal hydride species. Since hydricity is directly proportional to $E_{1/2}(M^{n+/(n-1)+})$, more hydridic hydrides can be accessed through synthetic strategies that employ ligands that are stronger electron donors.

Scheme 2. Hydricity in terms of BDFE and $E_{1/2}(M^{n+/(n-1)+})$.

$$[M\text{-}H]^{(n-1)+} \rightleftharpoons M^{(n-1)+} + H^\bullet \qquad \text{BDFE} \qquad (5)$$

$$M^{(n-1)+} \rightleftharpoons M^{n+} + e^- \qquad nFE_{1/2}(M^{n+/(n-1)+}) \qquad (6)$$

$$H^\bullet + e^- \rightleftharpoons H^- \qquad \Delta G^\circ_{H^\bullet/H^-} \qquad (7)$$

$$[M\text{-}H]^{(n-1)+} \rightleftharpoons M^{n+} + H^- \qquad \Delta G^\circ_{H^-} \qquad (1)$$

$$\Delta G^\circ_{H^-} = \text{BDFE} + nFE_{1/2}(M^{n+/(n-1)+}) + \Delta G^\circ_{H^\bullet/H^-} \qquad (8)$$

Of course, electrocatalytic CO_2 reduction can proceed by a variety of distinct mechanistic pathways, each resulting in different products, which is very clearly discussed by

Barlow *et al.* in a recent perspective article.[13] We describe herein the electrochemical reactivity of a recently-reported heteroleptic nickel complex bearing highly σ-donating N-heterocyclic carbenes (NHC's) to target reactive hydrides with CO_2. This work provides an illustration of competition between divergent pathways and the challenges associated with rational design of selective CO_2 reduction electrocatalysts.

RESULTS & DISCUSSION

Overview of the system studied. In an effort to probe and study the scaling relationship between hydricity ($\Delta G^\circ_{H^-}$) and the first reduction potential of the parent metal complex ($E_{1/2}(M^{n+/(n-1)+})$) we began exploring several N-heterocyclic carbene nickel complexes in conjunction with eq. 8 to target first-row transition metal hydrides capable of catalyzing the reduction of CO_2 to formate.[18-20] By this relationship, the hydricity of the metal hydride complex is predicted to increase with increasing electron density at the metal center; i.e. $\Delta G^\circ_{H^-}$ becomes more negative as $E_{1/2}(M^{n+/(n-1)+})$ becomes more negative. While nickel bis-diphosphine complexes would be a convenient starting point, we opted to investigate their heteroleptic analogues that feature the bis-NHC ligand: 1, l':3, 3'-bis(1,3-propanediyl)dibenzimidazolin-2,2′-diylidene, as even the most donating nickel bis-diphosphine complex $[Ni(dmpe)_2]^{2+}$ (dmpe = 1,2-Bis(dimethylphosphino)ethane) does not yield hydrides of sufficient reactivity to reduce CO_2 under standard conditions in acetonitrile.[8,

[21] Furthermore, the geometric constraints of the bis-NHC ligands allows synthesis of several heteroleptic nickel diphosphine complexes where further tuning of the electron density at nickel can be achieved.[20]

Scheme 3. Complex **1** and bis-NHC ligand.

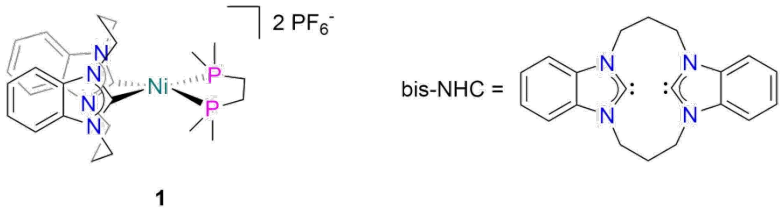

1

Estimation of the hydricity for complex **1** was obtained by application of eq. 8 using the fixed-slope line in our scaling relationship (Figure 1). Cyclic voltammograms of complex **1** (Figure 2) show a reversible two electron reduction at -1.87 V vs $Fc^{+/0}$ which predicts a hydricity for the corresponding hydride to be ~37.8 kcal mol^{-1}. Though these relationships are derived for complexes exhibiting distinct $E_{1/2}(M^{n+/(n-1)+})$ and $E_{1/2}(^{M(n-1)+/(n-2)+})$ couples and some additional uncertainty may be introduced in the case of a two-electron reduction as discussed in Ref. 17, this is in very reasonable agreement with the experimentally benchmarked value that was found to be less than 40.6 kcal mol^{-1}.[20] These values indicate that hydride transfer to CO_2 is thermodynamically favorable by at least ~3.4 kcal mol^{-1}. Furthermore, the hydride's pK_a can be estimated at ~33 by an analogous relationship described in Ref 17, consistent with protonation of the Ni(0) state by both phenol and methanol as described previously.[17, 20]

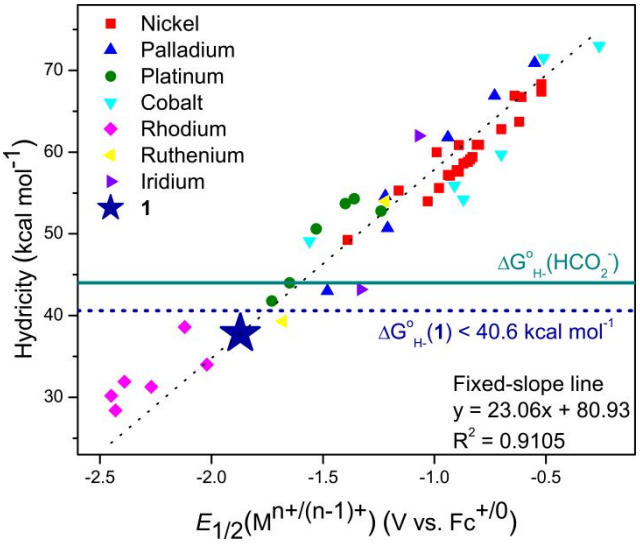

Figure 1. Plot of known hydricities of $d^{8/9}$ metals versus $E_{1/2}(M^{n+/(n-1)+})$ (adapted from ref. 17).[17] The hydricity of formate (44 kcal mol^{-1}) is indicated by the cyan line. The predicted hydricity of **1** (based on the fixed-slope line) and the experimentally-determined upper bound thereof are denoted by the blue star and dashed line, respectively.

Electrocatalytic CO_2 Reduction. In the presence of phenol, **1** shows significant current enhancement at the Ni(II/0) couple which corresponds to hydrogen evolution with 100% FE (Figure 2b).[20] Interestingly however, upon the introduction of a CO_2 atmosphere, a significant change in the electrocatalytic response is observed (Figure 2a), indicative of either an entirely different catalytic process or the emergence of a competing process. The electrocatalytic current is significantly reduced in the presence of CO_2, exhibiting a decrease in i_{cat}/i_p from 13.8 at 0.4 M phenol under N_2 to 9.34 at 0.4 M phenol under CO_2, where i_{cat} and i_p correspond to the plateau catalytic current and the peak current in the absence of substrate, respectively.[22]

This suggests that the competing process is slow with respect to the hydrogen evolution observed in the presence of phenol under an inert atmosphere or simply blocks it from proceeding.

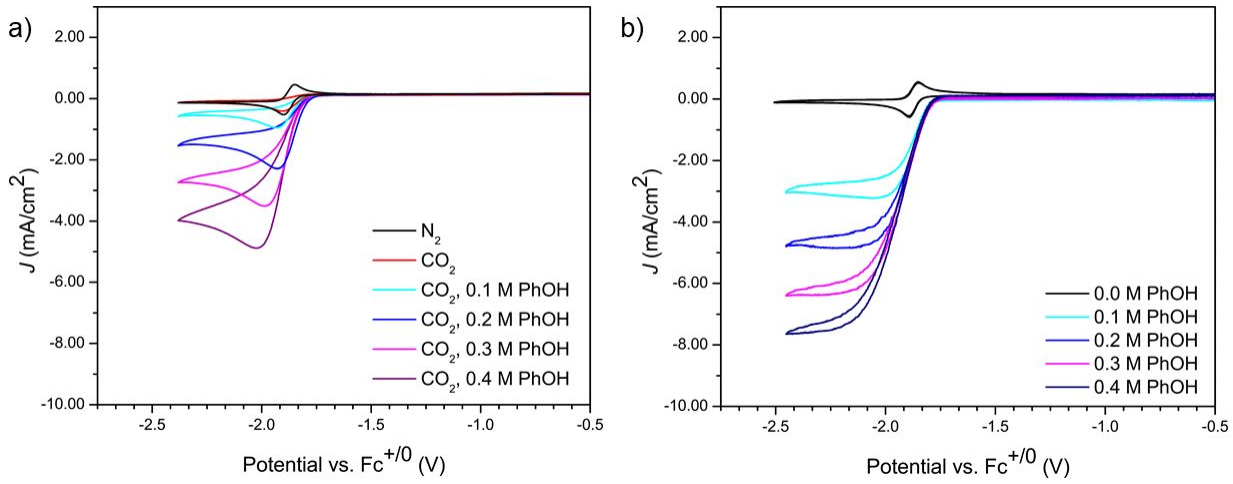

Figure 2. a) Cyclic voltammograms of **1** (1 mM) in the presence of phenol (up to 0.4 M) under an atmosphere of CO_2. Conditions: 0.1 M Bu_4NPF_6 in acetonitrile saturated with CO_2 at 100 mV s^{-1}; glassy carbon working electrode; platinum counter electrode; Ag/AgCl reference electrode. **b)** Cyclic voltammograms of **1** (1 mM) in the presence of phenol (up to 0.4 M) under an atmosphere of N_2. Conditions: 0.1 M Bu_4NPF_6 in acetonitrile at 100 mV s^{-1}; glassy carbon working electrode; platinum counter electrode; Ag/AgCl reference electrode.

Secondly, introduction of a CO_2 atmosphere results in a significant change in the shape of the catalytic wave, suggesting a kinetically distinct catalytic process. In the absence of CO_2, the catalytic wave exhibits near ideal S-shaped behavior, indicative of "pure kinetic"

conditions corresponding to fast catalysis unhindered by substrate consumption in the diffusion layer.[23] Conversely, a peak-shaped current response is observed under an atmosphere of CO_2, most often indicating substrate consumption or other "side phenomena" such as substrate inhibition or catalyst deactivation.[24, 25]

While the electrocatalytic response from the CVs under a CO_2 atmosphere would initially suggest the possibility of competitive hydride transfer to CO_2, yielding formate, CPE experiments performed under identical conditions at -1.75 V show only the production of CO and hydrogen at 25% and 55% FE respectively (Figures S1-S2). The remaining unaccounted passed charge is most likely due to catalyst degradation under these conditions (*vide infra*).

In order to suppress hydrogen evolution, methanol can be utilized as the added proton source to avoid protonation of the electrochemically-generated hydride. Addition of methanol followed by introduction of a CO_2 atmosphere yields mild current enhancement at the Ni(II/0) couple in conjunction with a disappearance of the hydride oxidation feature at -1.15 V vs. $Fc^{+/0}$. (Figure S3) And while CPE studies under these conditions demonstrate successful suppression of hydrogen evolution (FE_{H2} = 4%), generation of methoxide by deprotonation of methanol convolutes product analysis. Though trace formate (FE = 1%) and CO (FE = 22%) are observed upon electrolysis work up, (Figures S4-S6) methoxide is known to readily catalyze carbonylation of methanol to methyl formate in the presence of CO.[26] Therefore, due to the possibility of carbonylation activity and the degradation pathways of **1** discussed herein (*vide infra*), we refrain from assigning observed formate to be a result of hydride transfer to CO_2.

However, the significant production of CO in the presence of phenol indicates reactivity of the Ni(0) state directly with CO_2, which is typical of other systems such as $[Ni(cyclam)]^{2+}$, which has been shown to bind CO_2 upon reduction of the nickel center followed by reductive disproportionation to generate CO.[27] Indeed, cyclic voltammograms of **1** under CO_2 in the absence of a proton source result in a complete loss in reversibility of the Ni(II/0) couple with no observable increase in current. (Figure 3) This response is consistent with electron transfer to the catalyst followed by a chemical step (EC). In this system, the chemical step is believed to be irreversible binding of CO_2 to the electrochemically-generated, charge-neutral Ni(0) state. As discussed subsequently, this results in rapid degradation of the complex, likely circumventing truly catalytic behavior towards CO_2.

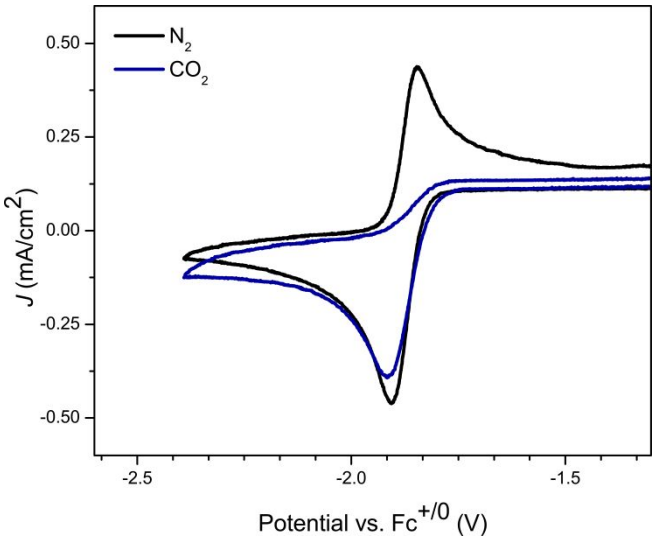

Figure 3. Cyclic voltammograms of **1** (1 mM) with no added proton source under nitrogen (black) and under CO_2 (blue). Conditions: 0.1 M Bu_4NPF_6 in acetonitrile at 100 mV s^{-1}; glassy carbon working electrode; platinum counter electrode; Ag/AgCl reference electrode.

Infrared Spectroelectrochemistry. Infrared spectroelectrochemical (IR-SEC) studies of this reaction indicate that upon reduction, **1** directly binds CO_2 to leading to the formation of a Ni(0) dicarbonyl species in both the presence and absence of an added proton source. In the absence of an added proton source, upon scanning to –1.8 V vs. a Ag pseudoreference electrode intense bands at 1951 and 1881 cm^{-1} are observed to grow in coinciding with the growth of an additional set of bands at 1686, 1648, and 1608 cm^{-1}.

We assign the bands at 1951 and 1881 cm^{-1} to the formation of a $[Ni(bis\text{-}NHC)(CO)_2]^0$ species, which is consistent with the A_1 and B_1 ν(CO) modes in the expected C_{2V} geometry (Figure S7). This assignment is supported by previously reported Ni(0) dicarbonyl disphosphine complexes where the A_1 and B_1 ν(CO) modes are observed in a similar vicinity.[28, 29] The bands at 1686, 1648, and 1608 cm^{-1} however, most likely correspond to formation of a bicarbonate species generated by disproportionation of the Ni(0)–CO_2 adduct resulting in bicarbonate and the nickel carbonyl species. These observations are analogous to previous studies when $[Ni(cyclam)]^+$ is used as the catalyst.[27] Interestingly, formation of the nickel dicarbonyl species is still observed in the presence of phenol. (Figure S9) These findings suggest that binding of CO_2 to the Ni(0) state is a competitive pathway that persists, even in the

presence of a proton source and supports the observation of significant poisoning under catalytic conditions.

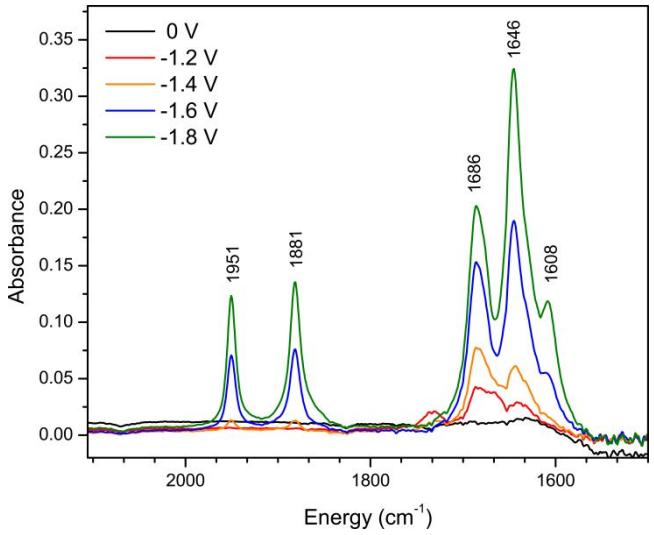

Figure 4. IR-SEC of **1** (3 mM) in CO_2-saturated acetonitrile in the absence of an added proton source, sweeping from 0 to -1.8 V vs. Ag pseudoreference electrode. Conditions: glassy carbon working electrode; platinum counter electrode; silver pseudoreference electrode; 0.1 M tetrabutylammonium hexafluorophosphate supporting electrolyte.

When the identical experiment was performed with $^{13}CO_2$ (Figure S8), a redshift of 46 and 41 wavenumbers is observed for the higher and lower energy ν(CO) modes, respectively. These findings are consistent with the expected isotopic shift for the generation of [Ni(bis-NHC)(^{13}CO)$_2$]^0. These findings are further supported by density functional theory (DFT) calculations. At the B3LYP level of theory, the DFT simulated FTIR spectrum of the [Ni(bis-

NHC)$(CO)_2]^0$ (Figure S7), is in striking agreement with the experimental FTIR spectrum, with ν(CO) modes at 1901 and 1838 cm^{-1}.

Computational Studies. Attempts to chemically isolate the doubly reduced state $\mathbf{1^0}$ and the hydride complex $\mathbf{1^H}$ were unsuccessful and we therefore employed DFT calculations to support their predicted geometries and qualitative molecular orbital structures. Calculations were carried out for complexes **1**, $\mathbf{1^0}$, and $\mathbf{1^H}$ using Restricted Kohn-Sham (RKS) calculations in the ORCA software suite (version 3.0.3) at the B3LYP level of theory. Further details on computational studies including input files and optimized coordinates are provided in the Supporting Information.

We previously reported the structural characterization of **1** and the phenyl-substituted analogues of both **1** and $\mathbf{1^0}$, [Ni(bis-NHC)(dppe)]$^{2+}$ and [Ni(bis-NHC)(dppe)]^0, respectively (dppe = 1,2-bis(diphenylphosphino)ethane).[20] The optimized structure of **1** shows the expected square planar geometry and is in close agreement with the solid state bond lengths (Table 2). The doubly reduced state, $\mathbf{1^0}$, is consistent with a tetrahedral Ni(0) d^{10} complex, which exhibits mild lengthening of 0.04 Å at the Ni-C bonds, and closely matches the crystallographic bond distances of the analogous tetrahedral [Ni(bis-NHC)(dppe)]^0 crystal structure.

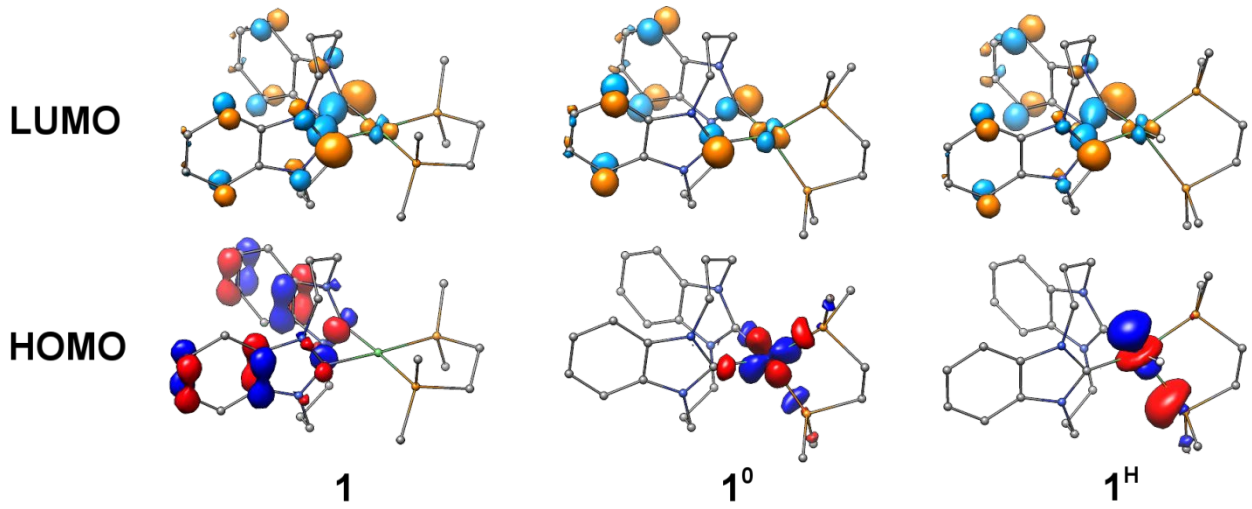

Figure 5. DFT-calculated HOMOs and LUMOs of complexes **1**, **1⁰**, and **1ᴴ**. Hydrogen atoms are omitted for clarity with the exception of the hydride of **1ᴴ**.

Table 1. Selected calculated and experimental bond lengths.

Bond	Complex					
	Calculated Bond Length (Å)			Crystallographic Bond Length (Å)[20]		
	1	**1⁰**	**1ᴴ**	**1**	[Ni(bis-NHC)(dppe)]$^{2+}$	[Ni(bis-NHC)(dppe)]^{0}
Ni-P1	2.20	2.20	2.17	2.1859(14)	2.2196(7)	2.1642(9)
Ni-P2	2.20	2.20	2.53	2.1710(14)	2.2063(7)	2.1643(8)
Ni-C1	1.92	1.96	1.91	1.900(4)	1.894(3)	1.921(3)
Ni-C2	1.92	1.96	1.94	1.899(5)	1.900(2)	1.914(3)
Ni-H	-	-	1.49	-	-	-

However, most notable is the optimized geometry and molecular orbital structure of $\mathbf{1^H}$, which adopts a distorted square pyramidal geometry with an associated τ_5 index of 0.21. The optimized structure provides direct insight into the observed instability of these species, displaying clear labilization of the phosphine ligand. The distorted 5-coordinate geometry exhibits significant lengthening of the Ni-P2 bond length from 2.20 Å in **1** and $\mathbf{1^0}$ to 2.53 Å in the calculated $\mathbf{1^H}$ structure. Investigation of the frontier orbital structure of this species reveals that the HOMO is antibonding in nature with respect to one of the phosphorus atoms of the dmpe ligand. The interaction consists of a d_{z^2}, nickel-based orbital in combination with an out-of-phase colinear phosphine σ orbital with calculated Mulliken reduced orbital populations of 47.0% at the nickel and 20.8% at the phosphorus. We postulate that this antibonding HOMO interaction results in instability of the 5-coordinate hydride species via labilization of the phosphine chelate, which yields susceptibility of attack at that position, leading to dissociation of the phosphine chelate.

Proposed Mechanism. Given these electrocatalytic and spectroscopic studies, we propose a series of divergent mechanistic pathways depicted in Scheme 4. All three possible pathways are initiated by the two-electron reduction of **1** to afford $\mathbf{1^0}$. Upon formation of $\mathbf{1^0}$, either direct interaction with CO_2 or protonation to form the proposed Ni(II) hydride $\mathbf{1^H}$ can occur. Protonation of $\mathbf{1^H}$ by a second equivalent of acid yields molecular hydrogen, regenerating **1**. Interestingly however, density function theory (DFT) studies indicate that $\mathbf{1^H}$ may be susceptible to phosphine labilization (*vide supra*). However, near ideal, S-shaped

catalytic responses observed in cyclic voltammetry experiments of **1** in the presence of phenol and stable current densities through several catalyst turnovers for HER in previous studies suggest that hydride protonation is fast with respect to hypothesized phosphine loss.[20]

Scheme 4. Proposed mechanistic pathways of CO_2 reduction and hydrogen evolution by **1**.

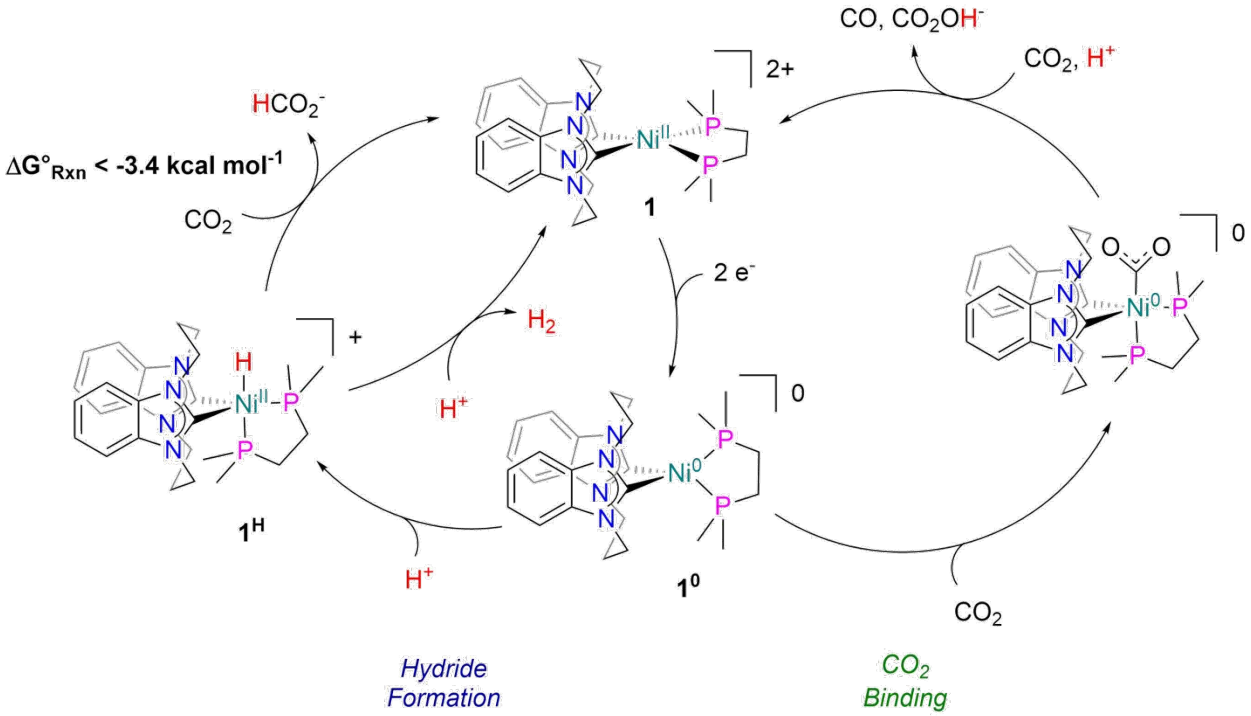

While the hydricity of $\mathbf{1^H}$ was experimentally benchmarked to be less than 40.6 kcal mol^{-1}, which establishes hydride transfer to CO_2 to be exergonic by at least 3.4 kcal mol^{-1}, no

significant formate was observed in controlled potential electrolysis experiments. Hydride transfer kinetics are generally quite slow at first row transition metals,[30-32] and we therefore postulate that fast protonation and instability of $\mathbf{1^H}$ preclude interaction of this species with CO_2 under catalytic conditions.

However, $\mathbf{1^0}$ readily reacts with CO_2 in both the presence and absence of an added proton source. Detection of CO as a reduction product in controlled potential electrolysis and spectroscopic observation of bicarbonate formation *via* IR-SEC experiments indicate a reductive disproportionation pathway, which is well established for $[Ni(cyclam)]^{2+}$ catalysts.[27] However, **1** suffers greatly from instability through this pathway as the CO-poisoned, dicarbonyl degradation product is observed by IR-SEC under an atmosphere of CO_2 at potentials negative of the Ni(II/0) couple both in the presence and absence of added acid.

Insights for future catalyst design. Directing selective electrocatalysis requires finely balancing catalyst intermediate reactivities, which becomes particularly convoluted when multiple substrates are required. Our focus over the course of these recent studies was to target strong hydricities at nickel to select for thermodynamically favorable hydride transfer to CO_2. However, tuning pre-catalyst redox couples to such negative potentials in the pursuit of reactive hydrides results in the generation of particularly electron-rich reduced states. In this case, the electrochemically-generated Ni(0) state becomes extremely nucleophilic, yielding direct binding of CO_2 to undergo reduction to CO in addition to deleterious catalyst poisoning.

This underscores the give-and-take nature of scaling relationships: the highly electron-rich catalyst sites required to access reactive hydride intermediates can in turn produce

divergent substrate reactivity and instability. In the case of **1**, stability issues may be remedied by the utilization of new ligand frameworks. While the bis-NHC ligand described herein successfully pushes reduction potentials at nickel to highly negative potentials, the instability of $\mathbf{1^H}$, may be a product of the orthogonal chelation geometry of this ligand, which we have shown previously to be quite rigid and pinched in comparison to typical 5-membered chelation motifs. However, even if greater stability of the hydride is achieved, the propensity for CO_2 binding at the reduced state of the catalyst would likely persist. Therefore, kinetic tuning to favor hydride formation over direct interaction with CO_2 through the installation of proton shuttles such as the well-studied P_2N_2 ligand family may represent a fruitful approach to improving pathway selectivity.However, a more elegant goal to develop new hydride transfer catalysts for CO_2 reduction would be to diverge from the hydricity scaling relationship altogether with the goal of accessing hydridic hydrides at milder potentials. Both kinetic approaches to direct reactivity and mechanisms by which divergence from the hydricity scaling relationship may be achieved are subjects of ongoing investigation in our laboratory.

CONCLUSION

Targeting catalysts for efficient and selective electrocatalytic reduction of CO_2 marks an important goal to improve fundamental mechanistic understanding of such catalytic processes. Homing in on the thermodynamic parameters governing hydride reactivity of catalyst intermediates with CO_2, we have established a route to electronically tune first-row hydrides to regimes capable of CO_2 reduction. However, we find that despite accessing

unprecedented hydricities at nickel, desired reactivity is circumvented by divergent mechanistic pathways. This not only underscores both the utility and limitation of thermodynamic scaling relationships in catalyst design, but also provides insight on the manner in which future design strategies may be steered to break from such relationships.

EXPERIMENTAL

General Considerations. All reactions were carried out under a nitrogen atmosphere using standard Schlenk and glovebox techniques. Solvents were sparged with argon, dried on a custom dry solvent system over alumina columns, and stored over molecular sieves before use. All reagents were obtained from commercial suppliers and used without further purification unless otherwise noted. Tetrabutylammonium hexafluorophosphate ($TBAPF_6$, Aldrich, 98%) was twice recrystallized from methanol and dried under a vacuum at 90°C overnight before use. **1** was prepared according to a previously-reported procedure.[20]

Instrumentation. ^{1}H NMR spectra were recorded on a Bruker 300 MHz spectrometer. ^{1}H NMR chemical shifts are reported relative to TMS ($\delta = 0$) and referenced against residual solvent proton peaks.

Electrochemistry. Electrochemical experiments were performed in 0.1 M tetra-n-butylammonium hexafluorophosphate solution in acetonitrile using a Gamry Reference 600 potentiostat. A single-compartment cell was used for cyclic voltammetry experiments with a glassy carbon working electrode (3 mm in diameter, Bioanalytical Systems, Inc.), Pt wire counter electrode, and Ag/AgCl pseudo-reference electrode. All potentials are referenced to

the $Fc^{+/0}$ couple using ferrocene as an internal reference. Controlled potential electrolysis experiments were carried out in a 5-port custom 90 mL cell with ground glass ports designed in our laboratory. The setup included a glassy carbon working electrode, graphite rod counter electrode separated from the solution by a porous glass frit, and Ag/AgCl pseudo-reference electrode separated from the solution by a Vycor tip. The counter and reference electrodes were housed in custom ground glass inserts which were sealed at the port with grease while the working electrode was connected via a wire protruding through a rubber septum. The remaining two ports were sealed with an additional two rubber septa, allowing for gas purging of the cell and headspace aliquots. For the catalytic electrolysis studies, the cell was charged with nickel catalyst (1 mM) and phenol (0.1 M) in 0.1 M tetra-n-butylammonium hexafluorophosphate solution in acetonitrile. Hydrogen and CO were quantified by analyzing 1 mL aliquots of the headspace on a Hewlett-Packard 7890A Series gas chromatograph with two molsieve columns (30 m × 0.53 mm ID × 25 μm film). The partial pressure of H_2 and CO in the headspace was determined by comparison to gas standard samples. Solution state product analysis was carried out by ^1H NMR. The post-electrolysis solution was decanted and the solvent was removed by rotary evaporation. The resulting mixture was extracted twice with D_2O, and an internal standard of a known quantity of maleic acid was added for NMR integration.

Infrared Spectroelectrochemistry. Infrared Spectroelectrochemistry (IR-SEC) was performed using a custom-built IR-SEC cell consisting of a 1 cm diameter glassy carbon working electrode, a Pt counter electrode, and Ag pseudo-reference electrode that have been

polished to a mirror finish.[33] Under an atmosphere of CO_2 or $^{13}CO_2$, the cell was loaded with an acetonitrile solution consisting of **1** (3 mM) and tetrabutylammonium hexaflourophosphate (0.1 M) and, when applicable, 0.1 M phenol. The potential of the IR-SEC cell was controlled using a Pine Instrument Co. Model AFCBP1 bipotentiostat. As the potential was scanned, thin layer bulk electrolysis was monitored by reflectance spectroscopy off of the polished glassy carbon electrode and infrared spectra were collected on a Bruker Equinox 55.

Computational Studies. Restricted Kohn-Sham (RKS) calculations were performed in the ORCA software suite (version 3.0.3) using the B3LYP functional with the RIJCOSX approximation. All carbon, hydrogen and nitrogen atoms were treated with Ahlrichs DEF2-SVP/J basis set while Ahlrichs DEF2-TZVP/J basis set was used for nickel and phosphorus. Dispersion corrections were applied using the Becke-Johnson damping scheme (D3BJ) and solvation was accounted for using the COSMO solvation model in acetonitrile.

CONFLICTS OF INTEREST

The authors declare no conflicts of interest.

ACKNOWLEDGEMENTS

This work was supported by the Joint Center for Artificial Photosynthesis, a DOE Energy Innovation Hub, supported through the Office of Science of the U.S. Department of Energy under Award No. DE-SC0004993.

REFERENCES

1. T. P. Senftle and E. A. Carter, *Acc. Chem. Res.*, 2017, **50**, 472-475.
2. R. C. Armstrong, C. Wolfram, K. P. de Jong, R. Gross, N. S. Lewis, B. Boardman, A. J. Ragauskas, K. Ehrhardt-Martinez, G. Crabtree and M. V. Ramana, *Nat. Energy*, 2016, **1**, 15020.
3. N. S. Lewis, *Science*, 2016, **351**, aad1920.
4. E. E. Benson, C. P. Kubiak, A. J. Sathrum and J. M. Smieja, *Chem Soc Rev*, 2009, **38**, 89-99.
5. P. De Luna, C. Hahn, D. Higgins, S. A. Jaffer, T. F. Jaramillo and E. H. Sargent, *Science*, 2019, **364**, eaav3506.
6. K. M. Waldie, F. M. Brunner and C. P. Kubiak, *ACS Sustainable Chemistry & Engineering*, 2018, DOI: 10.1021/acssuschemeng.8b00628, 6841-6848.
7. A. M. Lilio, M. H. Reineke, C. E. Moore, A. L. Rheingold, M. K. Takase and C. P. Kubiak, *J. Am. Chem. Soc.*, 2015, **137**, 8251-8260.
8. D. E. Berning, B. C. Noll and D. L. DuBois, *J. Am. Chem. Soc.*, 1999, **121**, 11432-11447.
9. C. J. Curtis, A. Miedaner, J. W. Raebiger and D. L. DuBois, *Organometallics*, 2004, **23**, 511-516.
10. E. S. Wiedner, M. B. Chambers, C. L. Pitman, R. M. Bullock, A. J. Miller and A. M. Appel, *Chem Rev*, 2016, **116**, 8655-8692.
11. B. R. Galan, E. S. Wiedner, M. L. Helm, J. C. Linehan and A. M. Appel, *Organometallics*, 2014, **33**, 2287-2294.
12. D. L. DuBois and D. E. Berning, *Applied Organometallic Chemistry*, 2000, **14**, 860-862.
13. J. M. Barlow and J. Y. Yang, *ACS Central Science*, 2019, **5**, 580-588.
14. B. M. Ceballos and J. Y. Yang, *Proceedings of the National Academy of Sciences*, 2018, **115**, 12686-12691.
15. C. Tsay, B. N. Livesay, S. Ruelas and J. Y. Yang, *J. Am. Chem. Soc.*, 2015, **137**, 14114-14121.
16. D. E. Berning, A. Miedaner, C. J. Curtis, B. C. Noll, M. C. Rakowski DuBois and D. L. DuBois, *Organometallics*, 2001, **20**, 1832-1839.

17. K. M. Waldie, A. L. Ostericher, M. H. Reineke, A. F. Sasayama and C. P. Kubiak, *ACS Catal.*, 2018, **8**, 1313-1324.
18. M. H. Reineke, M. D. Sampson, A. L. Rheingold and C. P. Kubiak, *Inorg. Chem.*, 2015, **54**, 3211-3217.
19. M. H. Reineke, T. M. Porter, A. L. Ostericher and C. P. Kubiak, *Organometallics*, 2018, **37**, 448-453.
20. A. L. Ostericher, K. M. Waldie and C. P. Kubiak, *ACS Catal.*, 2018, **8**, 9596-9603.
21. C. J. Curtis, A. Miedaner, W. W. Ellis and D. L. DuBois, *J. Am. Chem. Soc.*, 2002, **124**, 1918-1925.
22. A. J. B. a. L. R. Faulkner, *Electrochemical Methods*, Wiley, New York, 1980.
23. C. Costentin, M. Robert and J.-M. Savéant, *Chemical Society Reviews*, 2013, **42**, 2423-2436.
24. C. Costentin, S. Drouet, M. Robert and J.-M. Savéant, *J. Am. Chem. Soc.*, 2012, **134**, 11235-11242.
25. I. Bhugun and J. M. Saveant, *J. Electroanal. Chem.*, 1996, **408**, 5-14.
26. W. a. K. Reutemann, H., in *Ullmann's Encyclopedia of Industrial Chemistry*, 2000, DOI: 10.1002/14356007.a12_013.
27. J. D. Froehlich and C. P. Kubiak, *J Am Chem Soc*, 2015, **137**, 3565-3573.
28. J. Chatt and F. A. Hart, *Journal of the Chemical Society (Resumed)*, 1960, DOI: 10.1039/JR9600001378, 1378-1389.
29. C. Flener Lovitt, G. Frenking and G. S. Girolami, *Organometallics*, 2012, **31**, 4122-4132.
30. T.-Y. Cheng and R. M. Bullock, *Organometallics*, 1995, **14**, 4031-4033.
31. T.-Y. Cheng, B. S. Brunschwig and R. M. Bullock, *J. Am. Chem. Soc.*, 1998, **120**, 13121-13137.
32. T.-Y. Cheng and R. M. Bullock, *Organometallics*, 2002, **21**, 2325-2331.
33. C. W. Machan, M. D. Sampson, S. A. Chabolla, T. Dang and C. P. Kubiak, *Organometallics*, 2014, **33**, 4550-4559.

For TOC

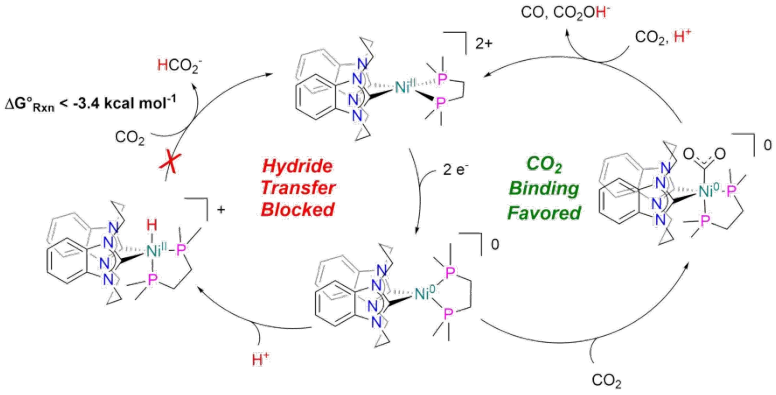
CO, CO2OH-
CO2, H+
2+
HCO2-
ΔG°Rxn < -3.4 kcal mol-1
CO2
Hydride
Transfer
Blocked
2 e-
CO2
Binding
Favored
0
+
0
H+
CO2